

Barotropic instability of a time-dependent parallel flow

Timour Radko[†]

Department of Oceanography, Naval Postgraduate School, Monterey, CA 93943, USA

(Received 2 January 2021; revised 6 June 2021; accepted 12 June 2021)

This study examines the long-wavelength instabilities of an inviscid parallel time-dependent current on the beta-plane. The basic flow is represented by the Kolmogorov pattern, the amplitude of which is modulated in time. Particular attention is given to the regime in which the corresponding steady flows are stable according to the Rayleigh–Kuo criterion. It is shown that the presence of a fluctuating component, regardless of how weak it may be, always renders the basic current linearly unstable. The destabilization is attributed to the resonant forcing of large-scale Rossby waves. The analysis is based on the asymptotic multiscale model, which is validated by numerical simulations. Since most geophysical flows are inherently time-dependent, the associated shear instabilities could represent a significant and ubiquitous source of barotropic turbulence.

Key words: geophysical and geological flows, instability

1. Introduction

Stability analyses of parallel laminar flows represent one of the oldest and most developed components of fundamental fluid mechanics. In the geophysical context, instabilities caused by lateral shears, commonly known as barotropic instabilities, strongly influence the circulation of tropical oceans, dynamics of the upper atmosphere and flow patterns on giant gas planets (e.g. Pedlosky 1987; Vallis 2006; Read *et al.* 2020). No attempt is made to review the entire field and the following discussion is focused on a subset of results that pertain directly to the present investigation.

The first physical insights into the instability of two-dimensional inviscid flows date back to the celebrated inflection-point theorem (Rayleigh 1880). This theorem states that parallel currents can be unstable only in the presence of an extremum of basic vorticity in the flow interior. The original formulation did not incorporate planetary rotation, which is known to affect the large-scale dynamics of most geophysical systems. Fortunately,

[†] Email address for correspondence: tradko@nps.edu

the Rayleigh theorem can be readily generalized for rotating configurations (Kuo 1949). The corresponding necessary instability condition is the existence of an extremum of the absolute vorticity Q^* – the asterisks hereafter denote dimensional variables – which includes both relative and planetary components. Thus, a steady zonal flow with basic velocity \bar{u}^* can be unstable only if the Rayleigh–Kuo condition

$$\frac{\partial Q^*}{\partial y^*} = \beta^* - \frac{\partial^2 \bar{u}^*}{\partial y^{*2}} = 0 \tag{1.1}$$

is met somewhere in the flow interior (y^* being the meridional coordinate). Equation (1.1) implies that the flow stability could be controlled by the meridional gradient of planetary vorticity, $\beta^* \equiv \partial f^* / \partial y^*$, commonly referred to as the beta-effect.

The Rayleigh–Kuo theorem represents one of the cornerstones of the classical stability theory. Yet, one can question whether the steady-state model of the basic flow, as natural and conventional as it may seem, captures all the essential dynamics. This concern becomes particularly relevant for oceanographic applications, in which most currents are inherently time-dependent. One of many examples is the system of alternating eastward and westward flows in tropical oceans (e.g. Godfrey *et al.* 2001; Johnson *et al.* 2002; Cravatte *et al.* 2012, 2017). This system exhibits significant variability on a wide range of temporal scales, which is driven by the changes in the wind stress, seasonal cycle and intrinsic time dependence associated with large-scale equatorial waves (e.g. Philander *et al.* 1986; Behera *et al.* 2013).

To explore the potential link between the unsteadiness of geophysical flows and their stability, we consider the canonical harmonic velocity pattern known as the Kolmogorov model (Meshalkin & Sinai 1961). The Kolmogorov framework affords attractive opportunities to develop explicit, dynamically transparent solutions representing the destabilization of laminar flows and transition to turbulence (e.g. Manfroi & Young 1999, 2002; Balmforth & Young 2002, 2005; Radko 2011a, 2014). A series of investigations (e.g. Sivashinsky 1985; Frisch *et al.* 1996) focused on marginally unstable regimes characterized by low Reynolds numbers, which afforded the development of analytical weakly nonlinear instability models. However, most large-scale geophysical applications are better represented by weakly dissipative or inviscid Kolmogorov-based solutions (e.g. Frenkel 1991; Borue & Orszag 1996; Lucas & Kerswell 2014; Lucas *et al.* 2017). This avenue of inquiry is pursued in our study as well. We develop an inviscid asymptotic model to examine linear properties of the barotropic time-dependent shear instabilities (BTSI hereafter). The nonlinear dynamics of BTSI is studied using high-resolution direct numerical simulations.

The present investigation is based on a particular type of the Kolmogorov model in which the amplitude of the basic velocity varies in time:

$$\bar{u}^* = (A^* + B^* \cos(\bar{\omega}^* t^*)) \sin(\bar{l}^* y^*). \tag{1.2}$$

Coefficients A^* and B^* in (1.2) represent the magnitudes of steady and fluctuating components, respectively. Our principal objective is the identification of instabilities in the regime where the basic current is stable according to the Rayleigh–Kuo criterion (1.1) throughout the entire period of oscillation,

$$\bar{l}^{*2} (|A^*| + |B^*|) < \beta^*. \tag{1.3}$$

The proposed model can be viewed as a generalization of the stability analyses of steady meridional Kolmogorov flows on the barotropic beta-plane (Manfroi & Young 1999, 2002) and oscillating basic states by Frenkel (1991) and Zhang & Frenkel (1998). However, it

also reveals a fundamentally different class of instabilities that emerge when the time dependence of the basic state and the beta-effect are considered concurrently. The origin of these instabilities is attributed to the resonant forcing of free Rossby waves by the oscillating basic state. The analogous dynamics has also been identified in studies of the inertial destabilization of zonal time-dependent equatorial flows (d’Orgeville & Hua 2005; Natarov *et al.* 2008). Another relevant example is the instability of time-dependent vertical shear flows in density-stratified fluids (Winters 2008; Radko 2019). In such systems, shears that are stable according to the Richardson number criterion (Richardson 1920; Howard 1961; Miles 1961) become unconditionally unstable due to the resonant forcing of internal gravity waves.

It should be emphasized that BTSI in our model are caused by the variation in the strength of the basic current. In this regard, they should be clearly distinguished from the instabilities of propagating monochromatic waves (Lorenz 1972; Gill 1974; Hua *et al.* 2008). Such structures can be rendered steady by using the coordinate systems moving with their zonal speeds. In contrast, the basic state (1.2) is fundamentally time-dependent and its temporal variability cannot be eliminated by a Galilean shift of the frame of reference. The irreducible time dependence of (1.2) is the singular reason for the instability of this flow pattern in the Rayleigh-stable parameter regime. The Rayleigh–Kuo theorem applies to steady flows, and this caveat proved to be critical. Nevertheless, some parallels could be drawn between the instabilities of plane waves and BTSI. For instance, Gill (1974) demonstrated that the instabilities of Rossby waves could be attributed to resonantly interacting triads – the mechanism that is also at work in the present model.

The analytical tractability in our study is achieved by considering the long-wavelength limit, in which the dominant spatial and temporal scales of perturbations greatly exceed those of the basic state. This regime is conveniently treated using techniques of the multiscale homogenization theory, a broad and active research area reviewed, for instance, by Mei & Vernescu (2010). The multiscale models typically assume simple small-scale patterns and explore their interaction with larger-scale structures using two sets of spatial and temporal variables (e.g. Gama *et al.* 1994; Novikov & Papanicolau 2001; Radko 2011*b,c*). The objective of such models is the derivation of explicit equations describing the evolution of large-scale fields. This goal is usually achieved by expanding governing equations in powers of a small parameter (ε) representing the ratio of small and large spatial scales. In our case, the multiscale model reveals that the basic state (1.2) is unstable for any finite amplitude ($B^* \neq 0$) of the time-dependent component.

The paper is organized as follows. The model configuration and the multiscale technique are described in § 2. Section 3 presents the detailed analysis of the solutions obtained for a purely oscillatory basic state ($A^* = 0$), which are subsequently generalized (§ 4) to include the finite steady component ($A^* \neq 0$). Section 5 presents a series of direct numerical simulations that illustrate the nonlinear evolution of instabilities. The results are summarized, and conclusions are drawn, in § 6.

2. Formulation

The starting point of this investigation is the forced barotropic vorticity equation

$$\frac{\partial \nabla^2 \psi^*}{\partial t^*} + J(\psi^*, \nabla^2 \psi^*) + \beta^* \frac{\partial \psi^*}{\partial x^*} = F^*, \quad (2.1)$$

where ψ^* is the streamfunction, associated with the velocity field $(u^*, v^*) = (-\partial \psi^* / \partial y^*, \partial \psi^* / \partial x^*)$, and J is the Jacobian. The term F^* represents external forcing, which maintains the time-dependent basic state (1.2). To reduce the number of controlling

parameters, the system is non-dimensionalized using $(\bar{l}^*)^{-1}$ as the unit of length, $(\bar{\omega}^*)^{-1}$ as the unit of time and $\bar{\omega}^*(\bar{l}^*)^{-2}$ as the unit of streamfunction. After non-dimensionalization, the vorticity equation reduces to

$$\frac{\partial \nabla^2 \psi}{\partial t} + J(\psi, \nabla^2 \psi) + \beta \frac{\partial \psi}{\partial x} = F, \tag{2.2}$$

where $\beta = \beta^*/\bar{\omega}^*\bar{l}^*$, and the basic state becomes

$$\bar{u} = (A + B \cos(t)) \sin(y), \tag{2.3}$$

where $(A, B) = (\bar{l}^*/\bar{\omega}^*)(A^*, B^*)$. The stability analysis of this system commences by linearizing (2.2) about the basic state (2.3) to obtain

$$\partial \nabla^2 \psi' / \partial t + J(\bar{\psi}, \nabla^2 \psi') + J(\psi', \nabla^2 \bar{\psi}) + \beta \frac{\partial \psi'}{\partial x} = 0, \tag{2.4}$$

where

$$\bar{\psi} = (A + B \cos(t)) \cos(y). \tag{2.5}$$

To investigate the interaction of pattern (2.5) with much larger scales of motion ($L_x, L_y \gg 1$), we introduce a small parameter

$$\varepsilon = \frac{2\pi}{L_y}, \tag{2.6}$$

which represents the ratio of the dominant meridional wavelengths of the large-scale perturbation and the basic state. This parameter is used to define the new set of spatial and temporal scales (X, Y, T), which are related to the original variables as follows:

$$X = \varepsilon^2 x, \quad Y = \varepsilon y, \quad T = \varepsilon^2 t. \tag{2.7a-c}$$

While the asymptotic ordering of the large-scale meridional variable (Y) follows directly from the definition of ε in (2.6), the identification of relevant large zonal scales is less trivial. We anticipate that the periodic variation in the basic state, which occurs on the $O(1)$ time scale, could resonate with free Rossby waves and induce their amplification. The dispersion relation of large-scale barotropic Rossby waves is

$$\omega = -\frac{\beta k}{k^2 + l^2}, \tag{2.8}$$

where ω is the frequency and (k, l) are the wavenumbers. Since by definition $l = \varepsilon$, $O(1)$ frequencies are realized for $k \sim \varepsilon^2$, which suggests scaling (2.7a) of the large-scale zonal variable X . The time scale T represents the relatively slow growth of large-scale patterns.

In the present configuration, we expect to find x -invariant solutions. This assumption can be rationalized by recalling that the basic state (2.5) does not vary in the zonal direction. Hence, its interaction with large-scale patterns is expected to generate secondary patterns that are also devoid of small-scale variability in x , and solutions of the governing equation

(2.4) are sought in five-dimensional space as

$$\psi' = \psi'(X, y, Y, t, T). \tag{2.9}$$

Thus, the derivatives in the governing equation (2.4) are replaced using

$$\frac{\partial}{\partial x} \rightarrow \varepsilon^2 \frac{\partial}{\partial X}, \quad \frac{\partial}{\partial y} \rightarrow \frac{\partial}{\partial y} + \varepsilon \frac{\partial}{\partial Y}, \quad \frac{\partial}{\partial t} \rightarrow \frac{\partial}{\partial t} + \varepsilon^2 \frac{\partial}{\partial T}, \tag{2.10a-c}$$

and both sets of variables are treated as independent variables. As a result, (2.10a-c) transforms (2.4) into

$$\begin{aligned} \frac{\partial \zeta'}{\partial t} + \varepsilon^2 \frac{\partial \zeta'}{\partial T} + \varepsilon^2 J_{Xy}(\bar{\psi}, \zeta') + \varepsilon^2 J_{Xy}(\psi', \bar{\zeta}) + \varepsilon^3 J_{XY}(\bar{\psi}, \zeta') \\ + \varepsilon^3 J_{XY}(\psi', \bar{\zeta}) + \beta \varepsilon^2 \frac{\partial \psi'}{\partial X} = 0, \end{aligned} \tag{2.11}$$

where J_{Xy} and J_{XY} are the Jacobians in (X, y) and (X, Y) , $\bar{\zeta} = \nabla^2 \bar{\psi}$ and $\zeta' = \nabla^2 \psi'$ are the basic and perturbation vorticities and

$$\nabla^2 \equiv \varepsilon^4 \frac{\partial^2}{\partial X^2} + \frac{\partial^2}{\partial y^2} + 2\varepsilon \frac{\partial^2}{\partial y \partial Y} + \varepsilon^2 \frac{\partial^2}{\partial Y^2}. \tag{2.12}$$

To explore the weak interaction between large-scale patterns and the basic flow, we consider the evolution of the plane wave

$$\psi_w = \hat{\psi}_w \exp\{i(KX + Y - \omega_0 t - \omega_2 T)\}, \tag{2.13}$$

where $K = k\varepsilon^{-2} = O(1)$ is the rescaled large-scale zonal wavenumber, ω_0 is the zero-order frequency and ω_2 is the correction induced by the weak interaction with the basic state (2.5). The imaginary component of the perturbation frequency measures the wave growth rate,

$$\lambda = \varepsilon^2 \text{Im}(\omega_2). \tag{2.14}$$

In the absence of the interaction with the basic state, the plane wave (2.13) would oscillate at the frequency

$$\omega = -\frac{\beta K}{K^2 \varepsilon^2 + 1}, \tag{2.15}$$

and the full-period resonance ($\omega = 1$) for $\varepsilon \rightarrow 0$ is expected to occur at $K \approx -\beta^{-1}$. However, to properly account for the wave interaction with the basic state, it becomes critical to explore a continuous range of values in the vicinity of the leading-order resonant wavenumber

$$K = -\beta^{-1}(1 + \delta \varepsilon^2), \tag{2.16}$$

where δ is an $O(1)$ quantity. The leading-order frequency of the plane wave is assumed to match that of the basic state,

$$\omega_0 = 1. \tag{2.17}$$

Another step that proved to be instrumental in reducing the number of controlling parameters is the renormalization of the basic state amplitude using

$$A = A_n \beta, \quad B = B_n \beta. \tag{2.18a,b}$$

The solution of the governing equations is now sought in terms of a power series in $\varepsilon \ll 1$,

$$\psi' = \psi_0(X, y, Y, t, T) + \varepsilon\psi_1(X, y, Y, t, T) + \varepsilon^2\psi_2(X, y, Y, t, T) + \dots \quad (2.19)$$

We substitute (2.19) into (2.11), collect terms of the same order in ε and sequentially solve the set of balances realized at each level in the expansion until an explicit expression for the growth rate (2.14) is obtained. The necessary solvability condition for this system is that the small-scale average of (2.11) is zero. This requirement applies to all orders in the expansion. However, as will be seen shortly, it is trivially satisfied at orders from the zeroth through the third. At the fourth order, however, the averaging over (y, t) yields the evolutionary equation for the large-scale component, which makes it possible to evaluate the growth rates of unstable modes. This procedure is illustrated first using the relatively simple case of a purely oscillatory basic state ($A = 0$) and then generalized (§ 4) to include a finite steady component ($A \neq 0$).

3. Oscillatory basic state ($A = 0$)

3.1. Multiscale expansion

The expansion opens with the large-scale plane wave (2.13), which is included in the leading-order component ψ_0 . It automatically satisfies the $O(1)$ and $O(\varepsilon)$ balances of the governing equation (2.11). However, we note that these balances are also satisfied by adding to ψ_w any slowly varying function g_0 of the form

$$g_0 = \hat{\psi}_w C_0 \cos(y) \exp\{i(KX + Y - \omega_2 T)\}. \quad (3.1)$$

Thus, we seek the solution for the $O(1)$ component of ψ' by assuming

$$\psi_0 = \psi_w + g_0, \quad (3.2)$$

with the expectation that the coefficient C_0 will be determined at a higher-order level in the expansion. Similarly, for the $O(\varepsilon)$ component of ψ' we consider the function

$$\psi_1 = \hat{\psi}_w C_1 \sin(y) \exp\{i(KX + Y - \omega_2 T)\}, \quad (3.3)$$

and its inclusion also satisfies the $O(\varepsilon)$ balance.

At the second order, we consider the solution of the form

$$\psi_2 = \psi_w (C_2^{(c)} \cos(t) + C_2^{(s)} \sin(t)) \cos(y). \quad (3.4)$$

The $O(\varepsilon^2)$ balance is satisfied as long as

$$C_0 = \frac{1}{2} \frac{B_n}{1 - \omega_2} \quad (3.5)$$

and

$$C_2^{(c)} = -\frac{B_n}{2} - iC_2^{(s)}. \quad (3.6)$$

The $O(\varepsilon^3)$ balance is characterized by the appearance of terms that are proportional to $\cos(2t)$, $\sin(2t)$, $\cos(2y)$ and $\sin(2y)$. This feature demands that we seek the third-order

component by assuming a more general structure

$$\begin{aligned} \psi_3 = \psi_w \sin(y) & (C_3^{(c)} \cos(t) + C_3^{(s)} \sin(t)) + \psi_w \sin(2y) (C_3^{(2c)} \cos(2t) \\ & + C_3^{(2s)} \sin(2t) + C_3^{(0)}). \end{aligned} \quad (3.7)$$

The $O(\varepsilon^3)$ balance is satisfied as long as

$$C_1 = \frac{iB_n \omega_2}{(\omega_2 - 1)^2} \quad (3.8)$$

and

$$C_3^{(c)} = i(B_n - C_3^{(s)}), \quad C_3^{(2c)} = \frac{iB_n^2}{16(\omega_2 - 1)}, \quad C_3^{(2s)} = \frac{B_n^2}{16(1 - \omega_2)}, \quad C_3^{(0)} = \frac{iB_n^2}{16(1 - \omega_2)}. \quad (3.9a-d)$$

The sought-after expression for the growth rate is obtained as a solvability condition, by averaging the $O(\varepsilon^4)$ balance in small-scale variables (y, t) :

$$\beta^2(3B_n^2 \omega_2 + 8\delta \omega_2^2 - 8\omega_2^3 + B_n^2 - 16\delta \omega_2 + 16\omega_2^2 + 8\delta - 8\omega_2) = 8(\omega_2 - 1)^2. \quad (3.10)$$

For given β and B_n , (3.10) implicitly determines $\omega_2(\delta)$. Thus, the identification of the most rapidly amplifying mode requires maximizing $\text{Im}(\omega_2)$ as a function of δ . This is accomplished by separating the complex frequency ω_2 into real and imaginary components:

$$\omega_2(\delta) = a(\delta) + ib(\delta), \quad (3.11)$$

where a and b are real quantities. We also isolate real and imaginary components of (3.10), resulting in

$$\begin{aligned} (-8 + (8\delta + 16)\beta^2)a(\delta)^2 + (24\beta^2 b(\delta)^2 + 16 + (3B_n^2 - 16\delta - 8)\beta^2)a(\delta) \\ - 8\beta^2 a(\delta)^3 + (8 + (-8\delta - 16)\beta^2)b(\delta)^2 - 8 + (B_n^2 + 8\delta)\beta^2 = 0 \end{aligned} \quad (3.12)$$

and

$$(-16 + (16\delta + 32)\beta^2)a(\delta) - 24\beta^2 a(\delta)^2 + 8\beta^2 b(\delta)^2 + 16 + (3B_n^2 - 16\delta - 8)\beta^2 = 0. \quad (3.13)$$

To determine the maximum of $b(\delta)$, we differentiate (3.12) and (3.13) with respect to δ and simplify the result by insisting that $(\partial/\partial\delta)b(\delta) = 0$, which yields

$$\begin{aligned} 8\beta^2 a^2 - 24\beta^2 a^2 c + 2(-8 + (8\delta + 16)\beta^2)ac - 16\beta^2 a \\ + (24\beta^2 b^2 + 16 + (3B_n^2 - 16\delta - 8)\beta^2)c - 8\beta^2 b^2 + 8\beta^2 = 0 \end{aligned} \quad (3.14)$$

and

$$16\beta^2 a - 48\beta^2 ac + (-16 + (16\delta + 32)\beta^2)c - 16\beta^2 = 0, \quad (3.15)$$

where $c \equiv (\partial/\partial\delta)a(\delta)$.

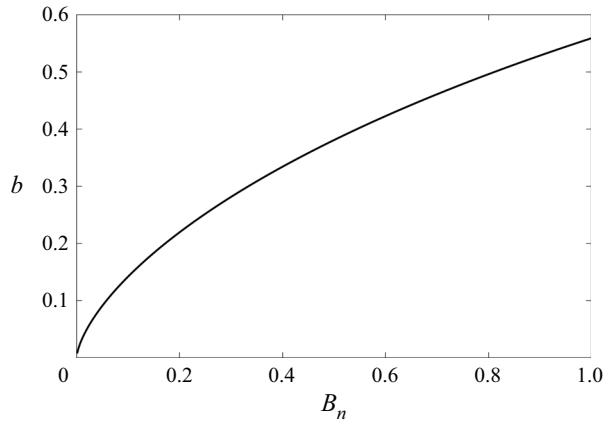


Figure 1. The rescaled growth rate, b , is plotted as a function of the parameter B_n , which controls the strength of the time-dependent component of the basic state, for the oscillatory model ($A = 0$).

The system of algebraic equations (3.12)–(3.15) can now be solved for any given (β, B_n) . First, we solve (3.15) for δ to get

$$\delta = \frac{\beta^2(3ac - a - 2c + 1) + c}{\beta^2c}, \tag{3.16}$$

and then we use (3.16) to eliminate δ in (3.12)–(3.14) in favour of (a, b, c) , obtaining

$$\left. \begin{aligned} (3B_n^2 + 24a^2 + 8b^2 - 48a + 24)c - 16(a - 1)^2 &= 0, \\ (16c - 8)a^3 - (48c - 24)a^2 + (3B_n^2c + 8b^2 + 48c - 24)a + B_n^2c - 8b^2 - 16c + 8 &= 0, \\ (3B_n^2 + 24a^2 + 24b^2 - 48a + 24)c - 8a^2 - 8b^2 + 16a - 8 &= 0. \end{aligned} \right\} \tag{3.17}$$

The elimination of δ produces an unexpected simplification. Remarkably, system (3.17) is independent of β , which implies that the solution is fully determined by the normalized amplitude of the basic flow B_n . The resulting relation $b(B_n)$ is shown in figure 1. Since the growth rate equations (3.17) are invariant with respect to the change in the sign of B_n , the results are presented only for $B_n \geq 0$. Figure 1 reveals the monotonic increase in the rescaled growth rate (b) with the normalized amplitude $|B_n|$. An even more significant finding is the unconditional instability ($b > 0$) of time-dependent oscillating zonal flows. This instability is realized even when the system is stable according to the Rayleigh–Kuo criterion (1.3), which in the present configuration ($A = 0$) reduces to $|B_n| < 1$.

The foregoing multiscale analysis indicates that the instability of time-dependent flows can be attributed to resonant triad interaction. The primary wave operating on frequencies that are close to that of the basic state (i.e. $\propto \cos(kx + ly - t - \varepsilon^2\omega_2t)$) interacts with the basic state $\cos(y)\cos(t)$ and produces, among other harmonics, the secondary mode proportional to $\sin(kx + ly + y - \varepsilon^2\omega_2t)$. This secondary mode itself interacts with the basic state and produces a component proportional to the primary mode. As a result, the primary mode amplifies. The multiscale model formalizes this interaction by identifying balances that arise at each order in ε and thereby explaining the chain of events leading to the instability.

3.2. Validation

At this stage, the multiscale analysis is complete and we can revert to the original variables using (2.6), (2.7a–c), (2.14) and (2.16), which yields the maximal growth rate

$$\lambda_{lin\ ms} = \frac{4\pi^2}{L_y^2} b(B_n) \tag{3.18}$$

and a corresponding zonal wavenumber of

$$k_{max} = -\frac{4\pi^2}{\beta L_y^2} \left(1 + \frac{4\pi^2}{L_y^2} \delta(\beta, B_n) \right). \tag{3.19}$$

To assess the accuracy of the foregoing asymptotic ($\varepsilon \rightarrow 0$) model (3.18), we now attempt to evaluate the growth rate numerically. This objective is accomplished by employing the zonally truncated model, in which

$$\psi' = \hat{\psi}_c(y) \cos(kx) + \hat{\psi}_s(y) \sin(kx). \tag{3.20}$$

We substitute (3.20) into the linearized vorticity equation (2.4) and isolate terms proportional to $\cos(kx)$ and $\sin(kx)$, resulting in

$$\frac{\partial}{\partial t} \begin{pmatrix} \frac{\partial^2 \hat{\psi}_c}{\partial y^2} - k^2 \hat{\psi}_c \\ \frac{\partial^2 \hat{\psi}_s}{\partial y^2} - k^2 \hat{\psi}_s \end{pmatrix} = L \begin{pmatrix} \hat{\psi}_c \\ \hat{\psi}_s \end{pmatrix}, \tag{3.21}$$

where L is a linear differential operator with time-dependent coefficients. The truncated system (3.21) was integrated in time using the Fourier spectral method (e.g. Radko 2014), which assumes periodic boundary conditions for $(\hat{\psi}_c, \hat{\psi}_s)$ at $y = 0, \Gamma_y$ and is based on the fourth-order Runge–Kutta time-stepping algorithm. In each of the following simulations, the extent of the computational interval (Γ_y) is assigned the value of the y -wavelength of the unstable mode, $L_y = 2\pi/\varepsilon$. We discretize the system using $N_y = 128(\Gamma_y/2\pi)$ grid points in y and initiate simulations by the random distribution of $(\hat{\psi}_c, \hat{\psi}_s)$. The growth rate is evaluated using the temporal record of the mean perturbation kinetic energy

$$e(t) = [\frac{1}{2} |\nabla \psi'|^2]_{xy}, \tag{3.22}$$

where $[\dots]_{xy}$ denotes the spatial average. A representative calculation of this type is shown in figure 2(a), which was performed for $B_n = 0.5, \beta = 1, \varepsilon = 0.2, \Gamma_y = 10\pi$ and $k = -0.0434$ – the latter was determined using (3.19). After the initial adjustment period, the perturbation starts to grow in a nearly exponential manner. The best linear fit to $\frac{1}{2} \ln(e)$ over the second half of the simulation ($10^3 < t < 2 \times 10^3$) yields the numerical estimate of the growth rate, $\lambda_{lin\ k} = 1.29 \times 10^{-2}$.

A series of calculations analogous to those in figure 2(a) was performed for $\Gamma_y = L_y = 2\pi n$, where $n = 3, 4, \dots, 10$. The resulting values of $\lambda_{lin\ k}$ are plotted as a function of $\varepsilon = 2\pi/L_y = 1/n$ in logarithmic coordinates in figure 2(b), along with the theoretical prediction (3.18). These calculations indicate that as ε decreases, the numerical and asymptotic results systematically converge. For $\varepsilon = 0.1$, these predictions differ by a mere 4%. Such agreement between the numerics and theory lends credence to the multiscale instability model.

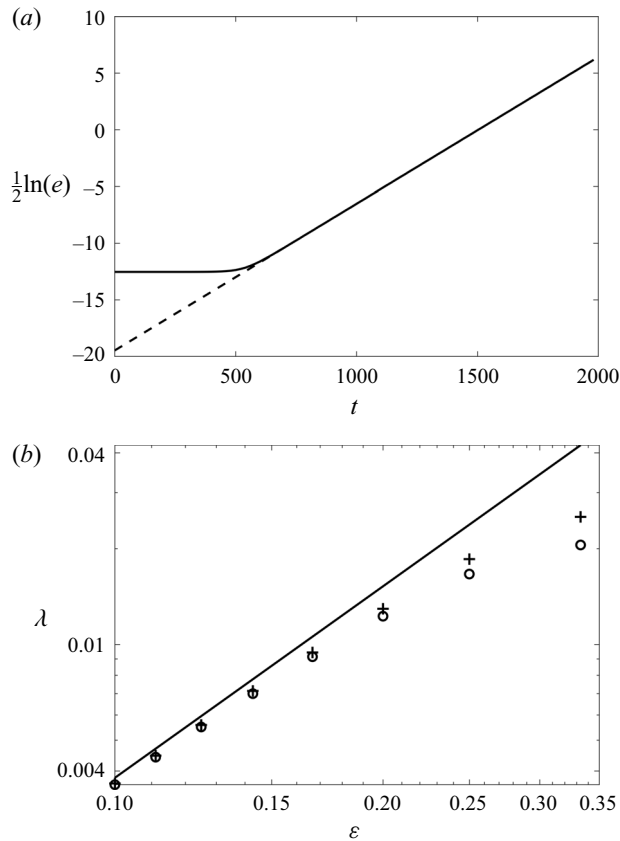


Figure 2. (a) The temporal record of $\frac{1}{2} \ln(e)$ obtained by the numerical integration of the truncated system (3.21) for $B_n = 0.5$, $\beta = 1$, $L_y = 10\pi$ and $|k| = 0.0434$. The numerical estimate of the growth rate ($\lambda_{num} = 1.29 \times 10^{-2}$) is determined from the best linear fit to this record over the second half of the integration interval. (b) The numerical estimates of the growth rate are plotted on the logarithmic scale as a function of $\varepsilon = 2\pi/L_y$ for $\beta = 1$ (plus signs) and for $\beta = 10$ (circles). The asymptotic prediction is indicated by the solid line.

An interesting property of BTSI revealed by the multiscale model is that the growth rate is uniquely determined by B_n . This surprising finding prompts the question of whether such invariance with respect to β is an exclusive feature of the long-wavelength approximation used in the multiscale theory. To address this possibility, a set of numerical calculations was performed with $\beta = 10$, which are also shown in figure 2(b). As expected, the growth rates for the different β are close for small ε , as both series approach the same asymptotic long-wavelength pattern. However, they visibly diverge for $O(1)$ wavenumbers.

4. Effects of a finite steady component ($A \neq 0$)

The foregoing multiscale model is now generalized by considering a basic state which contains a finite steady component. While this extension represents a significant step towards realism, particularly in the context of geophysical applications (§ 1), it also leads to substantial technical difficulties. The development of the multiscale theory generally follows that in § 3. However, in the special case of $A = 0$, a consistent asymptotic solution was obtained which involves only the two lowest harmonics in y . The principal complication in the finite- A case is caused by the excitation of an infinite series of Fourier

components in y . Therefore, the earlier theory was modified using the Galerkin projection method, in which the solution for ψ' is constructed using the N lowest harmonics in y . To find an appropriate solution, we insist that the substitution of the truncated series into the governing equation not project onto these low harmonics in y . The increase in N makes it possible to determine solutions with any desired accuracy.

While the leading-order streamfunction component is still given by (3.1) and (3.2), the first-order solution takes the form of

$$\psi_1 = \hat{\psi}_w \sum_{m=1}^N C_1^{(m)} \sin(my) \exp\{i(KX + Y - \omega_2 T)\}. \quad (4.1)$$

The $O(\varepsilon^2)$ and $O(\varepsilon^3)$ balances of the governing equation demand that the second- and third-order components of the streamfunction be represented by the following patterns:

$$\psi_2 = \psi_w (C_2^{(c)} \cos(t) + C_2^{(s)} \sin(t) + C_2^{(0)} \cos(y)) \quad (4.2)$$

and

$$\begin{aligned} \psi_3 = & \psi_w (C_3^{(c)} \cos(t) + C_3^{(s)} \sin(t)) \\ & + \psi_w \sum_{m=1}^N \sin(my) (C_3^{(2c)(m)} \cos(2t) + C_3^{(2s)(m)} \sin(2t) + C_3^{(0)(m)}). \end{aligned} \quad (4.3)$$

The coefficients C in (4.1)–(4.3) are determined by the Galerkin projection, and the solvability condition at $O(\varepsilon^4)$ yields the growth rate. The growth rate calculations have been performed for $N = 2, \dots, 5$. Offhand, one would expect these solutions to be accurate only for a large number of harmonics. Fortunately, our model is characterized by the remarkably rapid convergence of the solutions with increasing N . For instance, the relative difference between the growth rates evaluated for $(A_n, B_n, \beta) = (0.5, 0.25, 1)$ using $N = 3$ and $N = 4$ is 3.54×10^{-5} . The difference between the $N = 4$ and $N = 5$ models is only 1.47×10^{-5} . Thus, for most intents and purposes, it is safe to assume that the three-mode approximation fully represents the system dynamics. The coefficients of the streamfunction components in (4.1)–(4.3) and the resulting growth rate equation for $N = 3$ are listed in Appendix A.

As previously (§ 3), we find that the rescaled maximal growth rate (b) is uniquely determined by the normalized magnitude of the basic flow, measured by A_n and B_n . The resulting relation $b = b(A_n, B_n)$ is shown in figure 3. Since the growth rate is invariant with respect to the change in sign of A_n and B_n , the results are presented only for $A_n \geq 0$ and $B_n \geq 0$ without loss of generality. While growth rate pattern in figure 3 was obtained for $N = 3$, it is visually indistinguishable from its counterparts for $N = 4$ and $N = 5$. A notable feature of this calculation is the unconditional linear instability of the system. Particularly intriguing is the instability in the regime where the flow is stable according to the Rayleigh–Kuo criterion (1.3). When expressed in terms of A_n and B_n , this criterion reduces to

$$|A_n| + |B_n| < 1. \quad (4.4)$$

The corresponding region in the (A_n, B_n) parameter space is located below the dashed line in figure 3. Given the relatively high growth rates in this region, we anticipate that time-dependent Rayleigh-stable flows exhibit vigorous instability and transition to turbulence at fully nonlinear stages. This expectation will be confirmed shortly (§ 5) by direct numerical simulations.

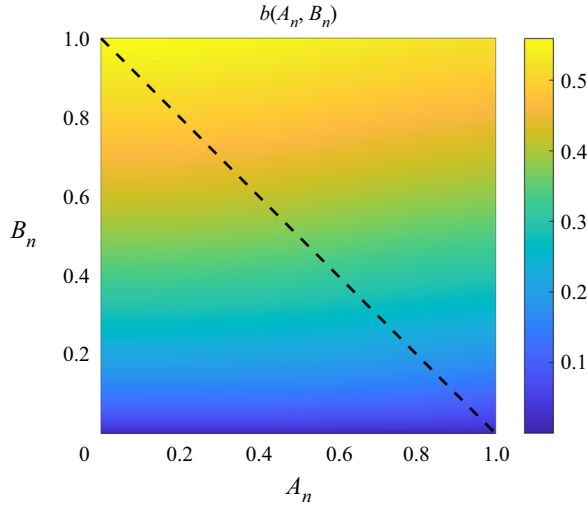


Figure 3. The rescaled growth rate, b , is plotted as a function of the parameters A_n and B_n , which control the strength of the basic current. The region below the dashed line represents the part of parameter space where the flow is stable according to the Rayleigh–Kuo criterion.

At this point, we revert to the original (small-scale) variables. The growth rate takes the form of

$$\lambda_{lin\ ms} = \varepsilon^2 b(A_n, B_n) = \frac{4\pi^2}{L_y^2} b(A_n, B_n), \tag{4.5}$$

and the corresponding zonal wavenumber is

$$k_{max} = -\beta^{-1} \varepsilon^2 (1 + \varepsilon^2 \delta(A_n, B_n, \beta)) = -\beta^{-1} \frac{4\pi^2}{L_y^2} \left(1 + \frac{4\pi^2}{L_y^2} \delta(A_n, B_n, \beta) \right). \tag{4.6}$$

The asymptotic result (4.5) has been validated by the truncated numerical model (3.21). Figure 4 presents a series of numerical integrations for $(A_n, B_n, \beta) = (0.5, 0.25, 1)$ and various values of L_y , revealing the convergence of the numerical and asymptotic estimates of λ with decreasing $\varepsilon = 2\pi/L_y$.

Another interesting property of BTSI is the contrast between the strong dependence of the rescaled growth rates (b) on B_n and their very weak dependence on A_n . This feature makes it possible to formulate simple empirical relations for the growth rate as a function of B_n only. For instance, the pattern in figure 3 can be approximated by the power-law relation

$$b_{fit} = DB_n^\alpha, \quad D = 0.5768, \quad \alpha = 0.6137, \tag{4.7a-c}$$

with a relative root-mean-square error of only 5.76%. For utilitarian purposes, it might prove useful to express this result in terms of dimensional quantities as

$$\lambda^* = \frac{4\pi^2 \bar{\omega}^*}{(L_y^* \bar{l}^*)^2} D \left(\frac{B^* \bar{l}^{*2}}{\beta^*} \right)^\alpha. \tag{4.8}$$

This empirical relation illustrates that the growth rate increases with the increasing frequency of oscillations ($\bar{\omega}^*$) and with decreasing β^* . The latter observation may seem

Barotropic instability of a time-dependent parallel flow

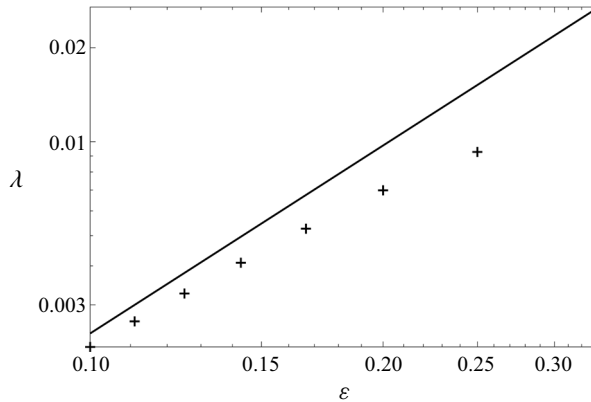


Figure 4. The growth rates are determined by the numerical integration of the truncated system (3.21) for $(A_n, B_n, \beta) = (0.5, 0.25, 1)$. These numerical estimates, indicated by the plus signs, are plotted on the logarithmic scale as a function of $\varepsilon = 2\pi/L_y$ along with the corresponding asymptotic prediction (solid line).

counterintuitive, considering that the instability mechanism is the resonant forcing of the Rossby waves that requires the beta-effect. Such a conundrum indicates that the multiscale model in its present form, which from the outset assumes $\beta = O(1)$, cannot properly represent the singular limit of $\beta \rightarrow 0$. This view is supported by the analysis of the non-rotating ($\beta = 0$) case, where the inviscid Kolmogorov flow with $A = 0$ is always stable (Frenkel 1991).

5. Direct numerical simulations

The foregoing linear analysis reveals the ubiquity of non-traditional barotropic instabilities of time-dependent shear flows, motivating efforts to explore their nonlinear development. This objective is addressed by performing a series of numerical simulations of the governing equation (2.2) using the Fourier-based spectral model (e.g. Sutyryn & Radko 2019). The model is de-aliased using the zero-padding algorithm and employs the fourth-order Runge–Kutta time-stepping scheme. To control the numerical stability of the code, (2.2) is augmented by the frictional term with a minimal viscosity of $\nu = 2 \times 10^{-4}$. The result is then expressed in terms of the perturbation streamfunction as follows:

$$\frac{\partial \nabla^2 \psi'}{\partial t} + J(\psi', \nabla^2 \bar{\psi}) + J(\bar{\psi}, \nabla^2 \psi') + J(\psi', \nabla^2 \psi') + \beta \frac{\partial \psi'}{\partial x} = \nu \nabla^4 \psi'. \quad (5.1)$$

The integrations of (5.1) were performed on a doubly periodic domain of size $(L_x, L_y) = (24\pi, 12\pi)$, which was resolved by $(N_x, N_y) = (4096, 2048)$ Fourier modes. The simulations were initialized by a small-amplitude random $\psi'(x, y)$ distribution. A typical experiment designed in this manner is shown in figures 5 and 6, where we present the perturbation streamfunction (ψ') and vorticity ($\zeta' = \nabla^2 \psi'$) fields, respectively. The governing parameters for this system ($A_n = 0.5$, $B_n = 0.25$) place it in the category of Rayleigh-stable flows, and therefore the amplification of perturbations is attributed exclusively to the BTSI dynamics.

The evolution of the flow field in this simulation is representative of most laminar-turbulent transition problems. After the adjustment period ($t \lesssim 200$), unstable modes emerge from the random initial perturbation field and start to amplify (figures 5a and 6a). These modes nonlinearly equilibrate by $t \sim 500$ (figures 5b and 6b), and their

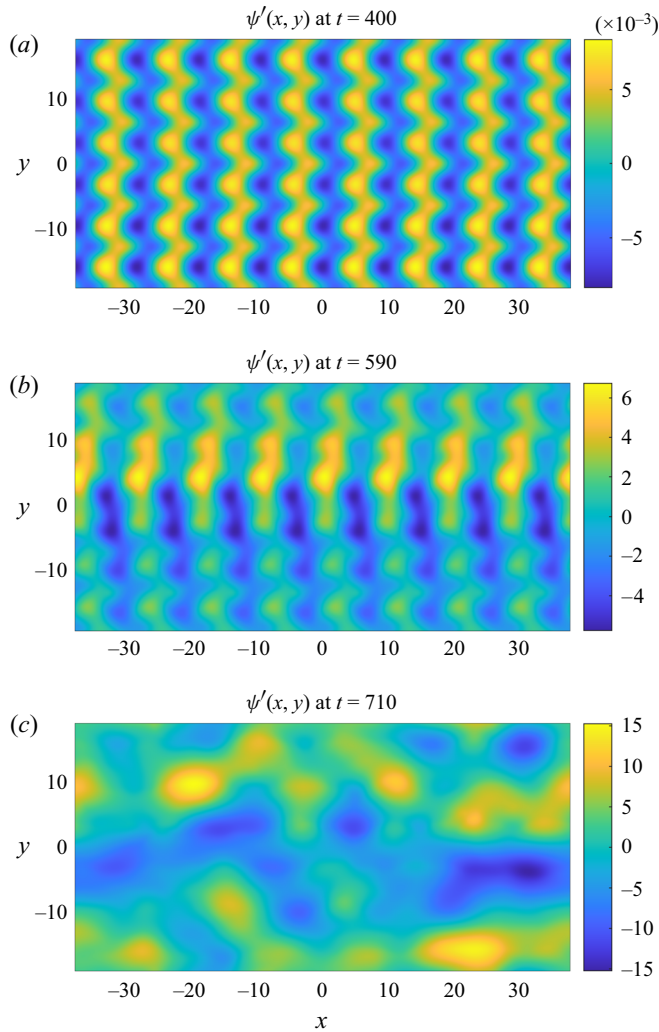


Figure 5. Direct numerical integrations of (5.1). The instantaneous perturbation streamfunction (ψ') fields are shown at various times in (a–c). The experimental parameters are $A_n = 0.5$, $B_n = 0.25$, $\beta = 1$, $\Gamma_x = 24\pi$, $\Gamma_y = 12\pi$, $N_x = 4096$ and $N_y = 2048$.

subsequent evolution is characterized by the development of chaotic and disorganized patterns. Finally, after $t \sim 700$, the flow field starts to exhibit a wide range of spatial scales (figures 5c and 6c), which is an expected manifestation of fully developed turbulence. The streamfunction field (figure 5c) is dominated by large-scale structures, the lateral extent of which is comparable to the size of the computational domain. However, the corresponding vorticity field (figure 6c) reveals the presence of small-scale patterns directly controlled by explicit friction.

Figure 7 illustrates the temporal variability of the spatially averaged perturbation energy (3.22) and enstrophy

$$r = [\frac{1}{2}(\zeta')^2]_{xy}, \tag{5.2}$$

Barotropic instability of a time-dependent parallel flow

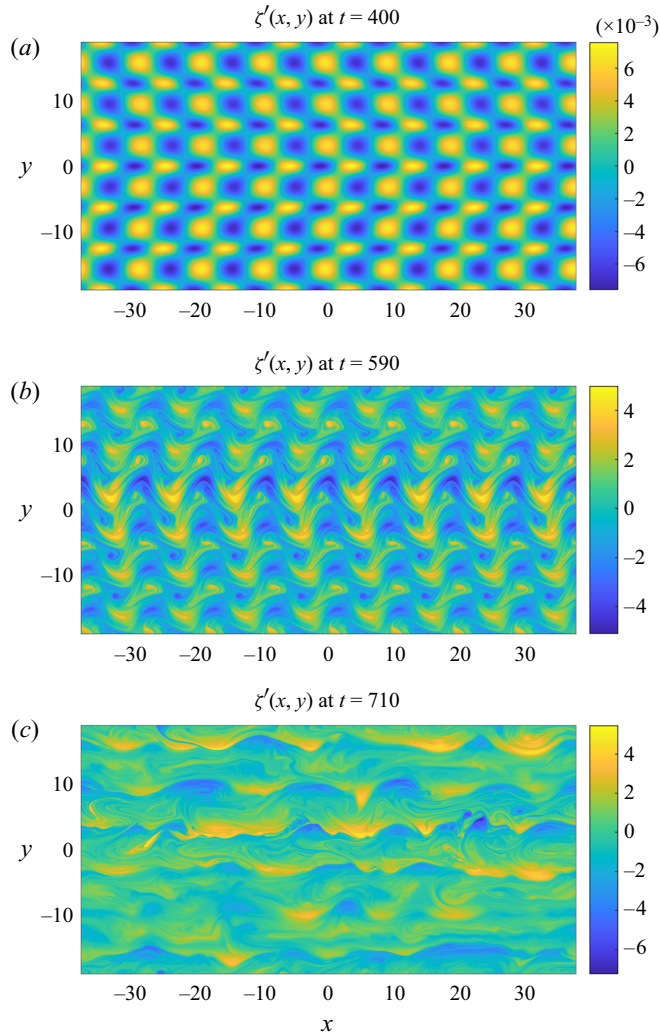


Figure 6. The same as figure 5 but for the vorticity perturbation $\zeta' = \nabla^2 \psi'$.

diagnosed from four simulations with various (A_n, B_n) . The experiments presented were performed with $A_n = 0.5, B_n = 0.25$ (EXP1); $A_n = 0.25, B_n = 0.25$ (EXP2); $A_n = 0, B_n = 0.5$ (EXP3); and $A_n = 0.25, B_n = 0.5$ (EXP4). The time series of energy (figure 7a) and enstrophy (figure 7b) are characterized by nearly exponential initial growth and subsequent equilibration at finite statistically steady levels. The system behaviour is sensitive to the values of B_n . The growth rates and the equilibrium levels of e and r substantially increase when the magnitude of the time-dependent component is raised from $B_n = 0.25$ (EXP1 and EXP2) to $B_n = 0.5$ (EXP3 and EXP4).

On the other hand, the influence of the steady component (A_n) on the system dynamics is rather limited. The time series of the energy and enstrophy generated for the same B_n but different values of A_n are generally similar. Such a strong (weak) dependence of fully nonlinear solutions in figure 7 on $B_n(A_n)$ is consistent with the properties of linear long-wavelength solutions in § 4 (e.g. figure 3).

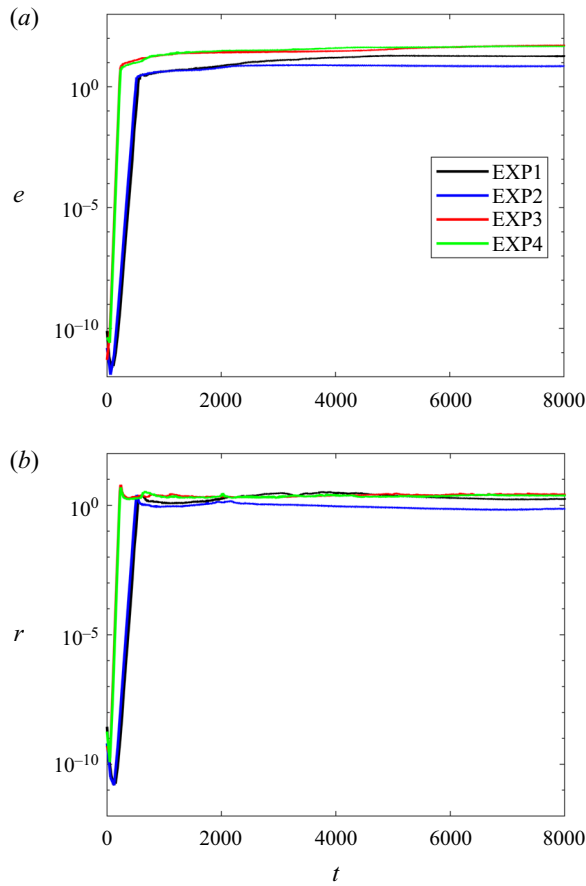


Figure 7. The temporal records of the spatially averaged perturbation energy (e) and enstrophy (r) are plotted on the logarithmic scale. The experiments performed with $(A_n, B_n) = (0.5, 0.25)$, $(0.25, 0.25)$, $(0, 0.5)$ and $(0.25, 0.5)$ are shown in black, blue, red and green, respectively. In all simulations $\beta = 1$.

To ensure the mutual consistency of simulations in figure 7 and the foregoing (§§ 3 and 4) linear analyses, we find it instructive to compare the growth rates obtained using various methods (table 1). The growth rates in simulations (λ_{DNS}) were evaluated over the intervals of nearly exponential growth, defined by requiring $10^{-8} < e < 10^{-1}$. In each experiment, λ_{DNS} was determined from the best linear fit to $\frac{1}{2} \ln(e)$ over this interval. The linear growth rates were computed using two other methods: (i) integration of the linearized single-mode equations ($\lambda_{in k}$) using the technique described in § 3.2; and (ii) extrapolation of the multiscale model ($\lambda_{in ms}$). The advantage of the single-mode truncation model is that it makes no assumptions regarding the wavelength of unstable perturbations, whereas the multiscale theory only represents the long-wavelength limit.

The growth rate in the single-mode model was computed using the vertical scale of $\Gamma_y = 12\pi$ and $k = -2\pi j/\Gamma_x$, where $j = 1, 2, \dots$ and $\Gamma_x = 24\pi$, thus exactly matching the dimensions of the computational domain used in simulations. The growth rates obtained for various wavenumbers were then maximized, yielding $\lambda_{in k}$. This procedure concurrently provided the estimate of the corresponding wavenumber (k_{max}) of the most rapidly amplifying mode. In all configurations considered (table 1), the linear model agrees

	A_n	B_n	λ_{DNS}	$\lambda_{lin\ k}$	$ k_{max} $	ε	$\lambda_{lin\ ms}$
EXP 1	0.5	0.25	0.0675	0.0700	0.6667	0.6134	0.0914
EXP 2	0.25	0.25	0.0688	0.0701	0.6667	0.6137	0.0941
EXP 3	0	0.5	0.1422	0.1419	0.6667	0.6138	0.1420
EXP 4	0.25	0.5	0.1428	0.1395	0.6667	0.6105	0.1407

Table 1. The growth rates realized in the numerical simulations (λ_{DNS}) are listed along with the corresponding estimates based on the linear single-mode model ($\lambda_{lin\ k}$) and the multiscale theory ($\lambda_{lin\ ms}$).

well with simulations, with the relative difference between λ_{DNS} and $\lambda_{lin\ k}$ never exceeding 4 %.

It should be noted that in all cases, the wavenumbers yielding the maximal growth ($|k_{max}|$) are not particularly small (table 1). Hence, the ability of the multiscale long-wavelength theory to accurately represent the simulations can be readily questioned. It is therefore interesting to examine how well the multiscale model performs under such unfavourable conditions. To accomplish this task, the effective ε in each experiment was evaluated from k_{max} by inverting (4.6) and then $\lambda_{lin\ ms}$ was computed using (4.5). The precision of the multiscale model proved to be parameter-dependent. It performed remarkably well in EXP3 and EXP4, with a relative error of less than 2 %. In other experiments, the relative difference between λ_{DNS} and $\lambda_{lin\ ms}$ was much larger: 35 % (EXP1) and 37 % (EXP2). However, these results are neither surprising nor disappointing, given that the effective value of the expansion parameter there is $\varepsilon = 0.61$ – hardly a small number by any standards.

6. Discussion

This study explores the barotropic instability of time-dependent shear flows. The investigation is based on the multiscale linear stability analysis of the Kolmogorov pattern and the associated fully nonlinear simulations. All evidence consistently points to a profound influence of temporal variability of zonal currents on their stability. It is shown that the BTSI identified in this study can occur for any finite magnitude of the time-dependent component of the basic state.

The proposed model of BTSI attributes the destabilization to resonant triad interactions, resulting in the transfer of energy from the basic state to barotropic Rossby waves. Perhaps our most intriguing finding – with potentially far-reaching implications – is that vigorous instabilities, capable of producing fully developed turbulence, are realized even in the regime where flows are stable according to the Rayleigh–Kuo criterion. This result should be contrasted with the analysis of Frenkel (1991), who demonstrated that the oscillatory ($A = 0$) Kolmogorov flows in the inviscid f -plane model are always stable. Such a difference between the f -plane and beta-plane models is consistent with the central role played by the resonant Rossby waves in the BTSI dynamics. The configuration explored here therefore presents an interesting example of a system that is destabilized by the beta-effect, a stabilizing agent in most geophysical models (e.g. Gill 1974; Manfroi & Young 2002).

Since geophysical flows are inherently time-dependent, BTSI could be one of the significant sources of turbulence. For instance, it is instructive to apply our findings to the system of alternating zonal currents in the tropical oceans, which are separated by $2\pi/\bar{l}^* \sim 400$ km (e.g. Cravatte *et al.* 2012, 2017). A major component of their temporal variability is

represented by the annual oscillations ($\bar{\omega}^* = 2 \times 10^{-7} \text{ s}^{-1}$) with a typical variation in the velocity of $B^* \sim 5 \text{ cm s}^{-1}$, which corresponds to $B_n \sim 0.5$. The simulations in figure 7(a) performed for $B_n = 0.5$ suggest that the perturbation kinetic energy eventually equilibrates at $e \sim 40$. This value is equivalent to a dimensional kinetic energy of $e^* = (\bar{\omega}^*/\bar{l}^*)^2 e \sim 60 \text{ cm}^2 \text{ s}^{-2}$, which is representative of near-surface variability in much of the world ocean (e.g. Stammer & Wunsch 1998). The possibility of generation and maintenance of such levels of turbulence by BTSI motivates the efforts to further advance our understanding of their dynamics, properties and large-scale consequences.

The present study could be extended in several ways. Exploring various basic states beyond the canonical Kolmogorov pattern may provide insight into the generality and broad applicability of our findings. Another step towards realism could involve the transition from the present monochromatic forcing model to distributed frequency spectra, more representative of temporal variability of geophysical flows. Finally, the diagnostics of field observations and comprehensive operational models might help to quantify the global contribution of BTSI-induced turbulence to lateral mixing and heat transport in the oceans and the atmosphere.

Acknowledgements. The author thanks Drs N. Balmforth and J. Brown and the anonymous reviewers for helpful comments.

Funding. Support of the National Science Foundation (grant OCE 1828843) is gratefully acknowledged.

Declaration of interests. The author reports no conflict of interest.

Author ORCID.

Timour Radko <http://orcid.org/0000-0002-5682-280X>.

Appendix A. Truncated ($N = 3$) multiscale model

The leading-order streamfunction component in the multiscale model for arbitrary A takes on a form identical to that obtained in § 3 for the special case of $A = 0$. It is still represented by (3.1) and (3.2), where the coefficient C_0 is given in (3.5). The coefficients of the first-order streamfunction component (4.1) are as follows:

$$\left. \begin{aligned} C_1^{(1)} &= -\frac{iB_n(51A_n^2\omega_2 - 144\omega_2^3 - 3A_n^2 + 52\omega_2^2 - 4\omega_2)}{4(\omega_2 - 1)^2(6A_n^2 - 36\omega_2^2 + 13\omega_2 - 1)}, \\ C_1^{(2)} &= -\frac{iA_nB_n(9\omega_2 - 1)}{2(\omega_2 - 1)(6A_n^2 - 36\omega_2^2 + 13\omega_2 - 1)}, \\ C_1^{(3)} &= -\frac{3iA_n^2B_n}{4(\omega_2 - 1)(6A_n^2 - 36\omega_2^2 + 13\omega_2 - 1)}. \end{aligned} \right\} \quad (A1)$$

The second-order component takes form (4.2) and its coefficients are

$$C_2^0 = -A_n, \quad C_2^{(c)} = -\frac{B_n}{2} - iC_2^{(s)}, \quad (A2a,b)$$

and the third-order coefficients in (4.3) are

$$\left. \begin{aligned} C_3^{(c)} &= i(B_n - C_3^{(c)}), & C_3^{(2c)(1)} &= -\frac{3}{4}B_n C_1^{(2)}, & C_3^{(2s)(1)} &= -\frac{3}{4}iB_n C_1^{(2)}, \\ C_3^{(0)(1)} &= \frac{3}{4}B_n C_1^{(2)} + 2iA_n, & C_3^{(2c)(2)} &= -\frac{(4\omega_2 - 1)}{8A_n}B_n C_1^{(2)}, \\ C_3^{(2s)(2)} &= -i\frac{(4\omega_2 - 1)}{8A_n}B_n C_1^{(2)}, & C_3^{(0)(2)} &= \frac{(4\omega_2 - 1)}{8A_n}B_n C_1^{(2)}, \\ C_3^{(2c)(3)} &= -\frac{B_n C_1^{(2)}}{12}, & C_3^{(2s)(3)} &= -\frac{iB_n C_1^{(2)}}{12}, & C_3^{(0)(3)} &= \frac{B_n C_1^{(2)}}{12}. \end{aligned} \right\} \quad (\text{A3})$$

The procedure for determining the maximal growth rate closely follows the example presented in § 3. The key solvability condition is obtained by averaging the $O(\varepsilon^4)$ balance in small-scale variables:

$$\begin{aligned} &\beta^2(45A_n^2 B_n^2 \omega_2 + 48A_n^2 \delta \omega_2^2 - 48A_n^2 \omega_2^3 - 108B_n^2 \omega_2^3 - 288\delta \omega_2^4 + 288\omega_2^5 + 3A_n^2 B_n^2 - 96A_n^2 \delta \omega_2 \\ &+ 96A_n^2 \omega_2^2 + 3B_n^2 \omega_2^2 + 680\delta \omega_2^3 - 680\omega_2^4 + 48A_n^2 \delta - 48A_n^2 \omega_2 + 10B_n^2 \omega_2 - 504\delta \omega_2^2 + 504\omega_2^3 \\ &- B_n^2 + 120\delta \omega_2 - 120\omega_2^2 - 8\delta + 8\omega_2) + 288\omega_2^4 - 48A_n^2 \omega_2^2 + 96A_n^2 \omega_2 - 680\omega_2^3 - 48A_n^2 \\ &+ 504\omega_2^2 - 120\omega_2 + 8 = 0. \end{aligned} \quad (\text{A4})$$

Equation (A4) implicitly determines the relation $\omega_2(\delta)$. This relation is then maximized to determine the most rapidly amplifying mode using the technique outlined in § 3. The result is a set of three lengthy algebraic equations (not shown) in $(a, b, c) \equiv (\text{Re}(\omega_2), \text{Im}(\omega_2), \partial \text{Re}(\omega_2)/\partial \delta)$, which take the form

$$E_j(a, b, c, A_n, B_n) = 0, \quad j = 1, 2, 3. \quad (\text{A5})$$

This system represents the generalization of the corresponding result (3.17) for finite A . Importantly, the equations in (A5) are independent of β , which makes it possible to determine a unique relation for the rescaled growth rate as a function of A_n and B_n ,

$$b = b(A_n, B_n). \quad (\text{A6})$$

This relation is shown in figure 3.

REFERENCES

- BALMFORTH, N.J. & YOUNG, Y.-N. 2002 Stratified Kolmogorov flow. *J. Fluid Mech.* **450**, 131–167.
 BALMFORTH, N.J. & YOUNG, Y.-N. 2005 Stratified Kolmogorov flow. Part 2. *J. Fluid Mech.* **528**, 23–42.
 BEHERA, S.K., BRANDT, P. & REVERDIN, G. 2013 The tropical ocean circulation and dynamics. In *Ocean Circulation and Climate – A 21 Century Perspective* (ed. G. Siedler, S. Griffies, J. Gould & J. Church), pp. 385–404. Academic Press.
 BORUE, V. & ORSZAG, S.A. 1996 Numerical study of three-dimensional Kolmogorov flow at high Reynolds numbers. *J. Fluid Mech.* **306**, 293–323.
 CRAVATTE, S., KESSLER, W.S. & MARIN, F. 2012 Intermediate zonal jets in the tropical Pacific Ocean observed by Argo floats. *J. Phys. Oceanogr.* **42**, 1475–1485.
 CRAVATTE, S., KESTENARE, E., MARIN, F., DUTRIEUX, P. & FIRING, E. 2017 Subthermocline and intermediate zonal currents in the tropical Pacific Ocean: paths and vertical structure. *J. Phys. Oceanogr.* **47**, 2305–2324.
 FRENKEL, A.L. 1991 Stability of an oscillating Kolmogorov flow. *Phys. Fluids A* **3**, 1718–1729.
 FRISCH, U., LEGRAS, B. & VILLONE, B. 1996 Large scale Kolmogorov flow on the beta-plane and resonant wave interaction. *Physica D* **94**, 36–56.

- GAMA, S., VERGASSOLA, M. & FRISCH, U. 1994 Negative eddy viscosity in isotropically forced 2-dimensional flow – linear and nonlinear dynamics. *J. Fluid Mech.* **260**, 95–126.
- GILL, A.E. 1974 The stability on planetary waves on an infinite beta-plane. *Geophys. Fluid Dyn.* **6**, 29–47.
- GODFREY, J.S., JOHNSON, G., MCPHADEN, M.J., REVERDIN, G. & WIFFELS, S.E. 2001 The tropical ocean circulation. In *Ocean Circulation and Climate: Observing and Modeling the Global Ocean* (ed. G. Siedler, J. Church & J. Gould), pp. 215–246. Academic Press.
- HOWARD, L.N. 1961 Note on a paper of John W. Miles. *J. Fluid Mech.* **10**, 509–512.
- HUA, B., D'ORGEVILLE, M., FRUMAN, M., MENESGUEN, C., SCHOPP, R., KLEIN, P. & SASAKI, H. 2008 Destabilization of mixed Rossby gravity waves and the formation of equatorial zonal jets. *J. Fluid Mech.* **610**, 311–341.
- JOHNSON, G., SLOYAN, B., KESSLER, W. & MCTAGGART, K. 2002 Direct measurements of upper ocean currents and water properties across the tropical Pacific during the 1990s. *Prog. Oceanogr.* **52**, 31–61.
- KUO, H.L. 1949 Dynamic instability of two-dimensional nondivergent flow in a barotropic atmosphere. *J. Meteorol.* **6**, 105–122.
- LORENZ, E.N. 1972 Barotropic instability of Rossby wave motion. *J. Atmos. Sci.* **29**, 258–269.
- LUCAS, D., CAULFIELD, C.P. & KERSWELL, R.R. 2017 Layer formation in horizontally forced stratified turbulence: connecting exact coherent structures to linear instabilities. *J. Fluid Mech.* **832**, 409–437.
- LUCAS, D. & KERSWELL, R. 2014 Spatiotemporal dynamics in two-dimensional Kolmogorov flow over large domains. *J. Fluid Mech.* **750**, 518–554.
- MANFROI, A. & YOUNG, W. 1999 Slow evolution of zonal jets on the beta plane. *J. Atmos. Sci.* **56**, 784–800.
- MANFROI, A. & YOUNG, W. 2002 Stability of beta-plane Kolmogorov flow. *Physica D* **162**, 208–232.
- MEI, C.C. & VERNESCU, M. 2010 *Homogenization Methods for Multiscale Mechanics*. World Scientific Publishing.
- MESHALKIN, L. & SINAI, Y. 1961 Investigation of the stability of a stationary solution of a system of equations for the plane movement of an incompressible viscous fluid. *Z. Angew. Math. Mech.* **25**, 1700–1705.
- MILES, J.W. 1961 On the stability of heterogeneous shear flows. *J. Fluid Mech.* **10**, 496–508.
- NATAROV, A., RICHARDS, K. & MCCREARY JR, J.P. 2008 Two-dimensional instabilities of time-dependent zonal flows: linear shear. *J. Fluid Mech.* **599**, 29–50.
- NOVIKOV, A. & PAPANICOLAOU, G. 2001 Eddy viscosity of cellular flows. *J. Fluid Mech.* **446**, 173–198.
- D'ORGEVILLE, M. & HUA, B.L. 2005 Equatorial inertial-parametric instability of zonally symmetric oscillating shear flows. *J. Fluid Mech.* **531**, 261–291.
- PEDLOSKY, J. 1987 *Geophysical Fluid Dynamics*. Springer.
- PHILANDER, S.G.H., HURLIN, W.J. & PACANOWSKI, R.C. 1986 Properties of long equatorial waves in models of the seasonal cycle in the tropical Atlantic and Pacific Oceans. *J. Geophys. Res.* **91**, 14207–14211.
- RADKO, T. 2011a Mechanics of thermohaline interleaving: beyond the empirical flux laws. *J. Fluid Mech.* **675**, 117–140.
- RADKO, T. 2011b On the generation of large-scale structures in a homogeneous eddy field. *J. Fluid Mech.* **668**, 76–99.
- RADKO, T. 2011c Eddy viscosity and diffusivity in the modon-sea model. *J. Mar. Res.* **69**, 723–752.
- RADKO, T. 2014 Applicability and failure of the flux-gradient laws in double-diffusive convection. *J. Fluid Mech.* **750**, 33–72.
- RADKO, T. 2019 Instabilities of a time-dependent shear flow. *J. Phys. Oceanogr.* **49**, 2377–2392.
- RAYLEIGH, LORD 1880 On the stability, or instability, of certain fluid motions. *Proc. Lond. Math. Soc.* **11**, 57–70.
- READ, P., KENNEDY, D., LEWIS, N., SCOLAN, H., TABATABA-VAKILI, F., WANG, Y., WRIGHT, S. & YOUNG, R. 2020 Baroclinic and barotropic instabilities in planetary atmospheres: energetics, equilibration and adjustment. *Nonlinear Process. Geophys.* **27**, 147–173.
- RICHARDSON, L.F. 1920 The supply of energy from and to atmospheric eddies. *Proc. R. Soc. A* **97**, 354–373.
- SIVASHINSKY, G. 1985 Weak turbulence in periodic flows. *Physica D* **17**, 243–255.
- STAMMER, D. & WUNSCH, K. 1998 Temporal changes in eddy energy of the oceans. *Deep-Sea Res. II* **46**, 77–108.
- SUTYRIN, G.G. & RADKO, T. 2019 On the peripheral intensification of two-dimensional vortices in a small-scale randomly forced flow. *Phys. Fluids* **31**, 101701.
- VALLIS, G.K. 2006 *Atmospheric and Oceanic Fluid Dynamics*. Cambridge University Press.
- WINTERS, K.B. 2008 Growth of inertia-gravity waves in sheared inertial currents. *J. Fluid Mech.* **601**, 85–100.
- ZHANG, X. & FRENKEL, A.L. 1998 Large-scale instability of generalized oscillating Kolmogorov flows. *SIAM J. Appl. Maths* **58**, 540–564.